applied sciences

MDPI

Article

Bow Diving Planes in Submarines: Analytical Sensitivity to Longitudinal Position and Finite-Element Assessment of Hull–Plane Connection Geometry

Arturo Silva-Campillo *, Miguel Angel Herreros-Sierra and Francisco Pérez-Arribas

Department of Naval Architecture, Shipbuilding and Ocean Engineering, Universidad Politécnica de Madrid (UPM), Avenida de la Memoria SN, 28040 Madrid, Spain
* Correspondence: a.silva@upm.es

Abstract

The positioning and geometry of submarine bow diving planes govern not only their contribution to pitch control but also the mechanical demand ultimately transmitted to the hull–plane connection. This study develops a sequential hydrodynamic–structural framework that traces this complete load path, from hydrodynamic force generation and pitching-moment authority to root bending and local connection stability. A conventional diesel–electric submarine is adopted as the reference configuration, combining analytical hydrodynamic formulations with finite-element assessment of the supporting structure. The results reveal that hydrodynamically equivalent solutions can produce markedly different structural consequences. Under the adopted linear formulation, a 10% increase in the longitudinal moment arm and a 10% increase in incidence provide the same relative increase in pitching moment; however, only the latter requires a proportional increase in transmitted force. Operating-condition sensitivity is dominated by local incident speed, whereas pressure-induced density variations between 50 and 300 m produce only a minor effect. Planform geometry introduces a further hydrodynamic–structural trade-off: increasing the equivalent aspect ratio from 4.00 to 6.25 reduces the incidence required for a prescribed pitching moment by approximately 12% while increasing root bending by 25%, despite an unchanged resultant lift. At the connection level, geometric redistribution and targeted stiffening outperform uniform thickness increases, with the most effective stiffening configuration increasing the elastic buckling metric by 83.8% while reducing structural weight relative to the thickest unstiffened bracket. These findings demonstrate that bow-plane design is fundamentally a load-path management problem, requiring longitudinal position, planform geometry, operating condition and connection architecture to be assessed as components of a single hydrodynamic–structural system.

Keywords: submarine; bow diving planes; hull–plane connection; structural response

Check for updates

Academic Editors: Zhaosheng Yu and Lei Wu

Received: 18 September 2026
Revised: 16 October 2026
Accepted: 27 October 2026
Published: 29 October 2026

Copyright: © 2026 by the authors. Licensee MDPI, Basel, Switzerland. This article is an open access article distributed under the terms and conditions of the Creative Commons Attribution (CC BY) license.

1. Introduction

The structural integration of control surfaces is an important aspect of submarine design, linking maneuvering requirements with the integrity of the supporting hull structure. Bow diving planes generate hydrodynamic forces that contribute to depth and pitch control, while their connections must transmit these forces to the hull through a localized structural assembly [1,2]. Their positioning therefore involves more than the selection of a suitable hydrodynamic lever arm: it also requires compatibility with the hull geometry, internal arrangement, and load-carrying capacity of the attachment region [3–5]. Understanding

the relationship between plane location and connection response is consequently relevant to the development of structurally efficient submarine configurations.

The longitudinal position of the bow diving planes determines the moment arm of their hydrodynamic force relative to the submarine center of gravity. Under otherwise equivalent loading conditions, increasing this distance increases the magnitude of the associated pitching moment [6]. However, this global effect must be distinguished from the local structural demand at the hull–plane connection. A larger moment arm about the submarine center of gravity does not, by itself, imply a larger bending moment at the plane root. The latter depends on the force distribution over the plane, the distance between the resultant load and the attachment, and the geometry and stiffness of the supporting assembly [7,8]. Consequently, the structural implications of repositioning the planes cannot be inferred solely from their contribution to pitch control.

Hydrodynamic investigations of submarine control surfaces provide a basis for evaluating force generation, control effectiveness, and interactions between appendages and the surrounding hull flow [9,10]. Parameters such as surface geometry, deflection, inflow conditions, and installation position are relevant to these assessments [11–14]. In particular, a change in longitudinal location may modify both the moment arm and the local flow experienced by the planes so that geometrically similar arrangements do not necessarily develop identical hydrodynamic forces [15,16]. These considerations establish the loading context for structural assessment, but the resulting response of the hull–plane connection also requires an explicit representation of the mechanical path through which those loads enter the submarine structure.

From a structural perspective, the attachment region constitutes a transition between the projecting control surface and the supporting hull. Differences in geometry and stiffness across this transition can produce nonuniform stress fields and localized deformation, whose magnitude depends on the configuration of the connection and its surrounding reinforcement [17]. Numerical methods, particularly finite element analysis, allow these effects to be examined by representing the interaction between the plane, its support, and the adjacent hull structure [18,19]. The interpretation of such analyses nevertheless depends on the assumptions used to prescribe loads and restraints. Comparisons between alternative arrangements therefore require consistent modeling criteria so that changes in structural response can be attributed to the configuration under investigation rather than to differences in numerical idealization [20,21].

The available installation region is also constrained by the overall submarine arrangement. The external hull form and the spatial distribution of tanks and internal systems may restrict the location and dimensions of the supporting assembly [22,23]. Tank capacities and filling conditions additionally contribute to the submarine mass distribution and can therefore affect the reference condition used to evaluate the moment arm of the diving planes [24]. These geometric and loading considerations should be distinguished: the tank arrangement defines part of the installation context, whereas its influence on the center of gravity depends on the specified loading condition. A consistent reference configuration is thus necessary when comparing the structural consequences of alternative plane positions.

Taken together, these considerations motivate a connection-level investigation of bow-plane positioning. Hydrodynamic effectiveness and local structural response describe different aspects of the same design decision, and neither can be used as a direct substitute for the other [25]. The question addressed here is how a change in the relative position of the bow diving planes affects the mechanical response of their connection to the hull when the reference submarine configuration and the comparison conditions are explicitly defined. Resolving this question requires separating the consequences of the adopted loading from those associated with the geometry and structural integration of the attachment.

The present study numerically investigates the influence of the relative position of bow diving planes on the structural behavior of the hull–plane connection in a reference submarine. The submarine geometry and tank arrangement establish the case-study configuration, while the plane and its supporting assembly define the structural region of interest. Alternative longitudinal positions are examined through an analytical sensitivity analysis, while a consistent finite-element modelling approach is employed to assess the influence of connection geometry and stiffening on the structural response of the reference configuration. The objective is to identify the structural implications of the positioning decision and to clarify the conditions under which the connection response becomes sensitive to the adopted arrangement. By focusing on the attachment rather than treating the diving plane solely as a hydrodynamic control surface, the investigation provides a basis for incorporating local structural performance into the assessment of bow-plane location.

2. Mathematical Background

The effect of the longitudinal position of the bow diving planes on the pitch response can be derived from the rigid-body moment balance about the submarine centre of gravity, G. Considering the longitudinal–vertical plane and adopting a body-fixed reference frame (x,z), the contribution of the hydrodynamic force generated by the bow planes to the pitching moment is obtained from

$$\mathrm{M}_G^{BP} = \mathrm{r}_{G,CP} \times \mathrm{F}_{BP} \tag{1}$$

Here, $\mathrm{r}_{G,CP}$ is the position vector from G to the centre of pressure of the bow planes and F_{BP} is the resultant hydrodynamic force. In the symmetry plane,

$$\mathrm{r}_{G,CP} = \begin{bmatrix} x_{BP} & 0 & z_{BP} \end{bmatrix}^T, \qquad \mathrm{F}_{BP} = \begin{bmatrix} X_{BP} & 0 & Z_{BP} \end{bmatrix}^T \tag{2}$$

The corresponding pitch-moment component is therefore

$$M_{BP} = z_{BP} X_{BP} - x_{BP} Z_{BP}. \tag{3}$$

In the operating conditions considered here, the axial-force contribution $z_{BP}X_{BP}$ is assumed to be small relative to the moment generated by the normal force. This approximation is justified when $|X_{BP}/Z_{BP}| \ll |x_{BP}/z_{BP}|$, leading to

$$M_{BP} \simeq -x_{BP} Z_{BP}. \tag{4}$$

The normal force generated by the planes is expressed as

$$Z_{BP} = \frac{1}{2} \rho U_e^2 S_{BP} C_{Z,BP}, \tag{5}$$

where ρ is the fluid density, U_e is the effective inflow velocity at the plane location, S_{BP} is the reference area and $C_{Z,BP}$ is the normal-force coefficient. Under a small-disturbance assumption, this coefficient can be linearised as

$$C_{Z,BP} \simeq C_{Z\alpha} \alpha_e + C_{Z\delta} \delta_{BP}, \tag{6}$$

where α_e is the local effective angle of attack, δ_{BP} is the plane deflection angle, and $C_{Z\alpha}$ and $C_{Z\delta}$ are the corresponding hydrodynamic derivatives. Substitution of Equations (5) and (6) into Equation (4) gives

$$M_{BP} \simeq -\frac{1}{2} \rho U_e^2 S_{BP} x_{BP} (C_{Z\alpha} \alpha_e + C_{Z\delta} \delta_{BP}). \tag{7}$$

Accordingly, the control derivative associated with bow-plane deflection is

$$M_{\delta_{BP}} = \frac{\partial M_{BP}}{\partial \delta_{BP}} \simeq -\frac{1}{2}\rho U_e^2 S_{BP} x_{BP} C_{Z\delta}. \tag{8}$$

A preliminary relationship between lift coefficient and angle of attack is established for the generic diving plane. The model assumes a symmetric, uncambered section operating at small angles of attack in attached flow. For a two-dimensional thin aerofoil, the sectional lift coefficient is approximated by [26]:

$$C_{Z\delta} \approx 2\pi\alpha \tag{9}$$

where α is expressed in radians and measured relative to the incident flow. As this two-dimensional relationship does not account for the finite span of the diving plane, a finite-span correction is therefore introduced through the lift-curve slope

$$C_L(\alpha) = a\alpha,\ a = \frac{a_0}{1 + \frac{a_0}{\pi e_a AR}} \tag{10}$$

Here, $a_0 \approx 2\pi$ rad^{-1} is the two-dimensional lift-curve slope, AR is the aspect ratio and e_a is an effective correction factor in the slope approximation. Taking $e_a = 1$ provides an idealised initial estimate; it is not a calibrated value for the proposed trapezoidal plane. As a first approximation to the root boundary condition, the hull is represented by a plane of symmetry.

Equation (8) shows that, provided that the local inflow conditions and plane geometry remain unchanged, pitch-control effectiveness varies linearly with the longitudinal distance between the centre of pressure of the bow planes and the submarine centre of gravity. Thus, increasing $|x_{BP}|$ increases the magnitude of the pitching moment generated for a given deflection. Nevertheless, an invariant force coefficient cannot generally be assumed when the longitudinal position is modified. Both the effective inflow velocity and the effective angle of attack depend on the local flow field around the hull. These quantities may be represented as

$$U_e = \kappa_U(x_{BP})U, \qquad \alpha_e = \alpha + \varepsilon(x_{BP}), \tag{11}$$

where U is the reference advance velocity, κ_U is the local velocity ratio and ε represents the position-dependent flow angularity induced by the hull. Consequently,

$$M_{BP} \simeq -\frac{1}{2}\rho U^2 S_{BP} x_{BP} \kappa_U^2(x_{BP})[C_{Z\alpha}(\alpha + \varepsilon(x_{BP})) + C_{Z\delta}\delta_{BP}] \tag{12}$$

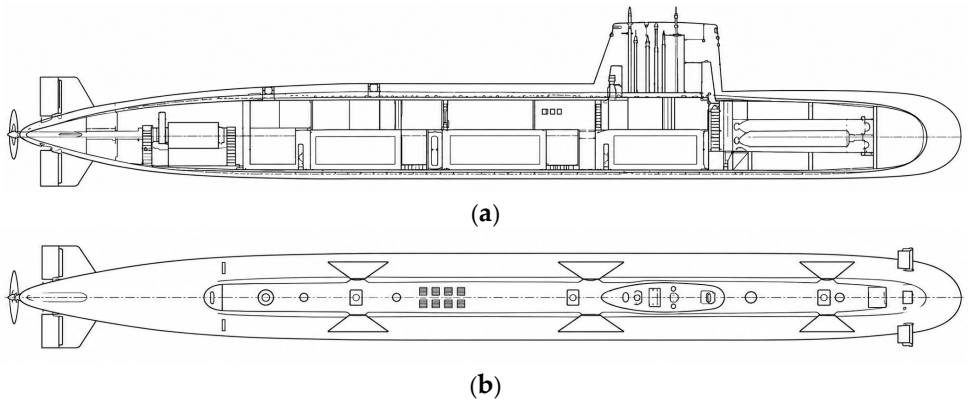
Equation (12) indicates that the longitudinal-position effect cannot, in general, be reduced exclusively to a geometric lever-arm variation. A change in x_{BP} may simultaneously alter the local dynamic pressure, the effective angle of attack and the hydrodynamic interaction between the planes and the hull. Therefore, the longitudinal location of the bow diving planes affects the pitch response through two coupled mechanisms: the variation in the moment arm relative to the centre of gravity and the modification of the local hydrodynamic conditions governing the force generated by the planes.

The present hydrodynamic formulation is intended as a simplified analytical model for comparative sensitivity assessment rather than as a validated prediction of the flow around an installed submarine diving plane. The adopted thin-airfoil approximation, finite-span correction and idealised hull-symmetry assumption do not resolve viscous effects or detailed hull–appendage interactions. Accordingly, the quantitative results are restricted to the specified modelling assumptions, and submarine-specific application would require validation against experimental measurements or higher-fidelity numerical simulations.

3. Case Study

3.1. Reference Submarine Geometry and Main Dimensions

The numerical model developed in this study is based on the main geometric characteristics of a conventional diesel–electric submarine. The vessel has an overall length of approximately 67.9 m and a maximum beam of 6.8 m. The external hull is characterised by a streamlined axisymmetric geometry, with a predominantly cylindrical central region connected to progressively tapered bow and stern sections. The draught in surfaced condition is approximately 5.4 m, while the corresponding displacement is approximately 1490 t, increasing to about 1750 t in submerged condition (Figure 1).



(**a**)

(**b**)

Figure 1. General arrangement. (**a**) Side view, (**b**) top view.

A Cartesian coordinate system is adopted to define the geometry and the relative position of the different structural components. The longitudinal axis, x, is aligned with the submarine centreline and oriented from aft to forward, whereas the transverse and vertical directions are represented by the y and z axes, respectively. For the purposes of the present numerical investigation, the origin of the coordinate system is located at the approximate centre of gravity (*CG*) of the submarine. As a first approximation, the longitudinal position of the *CG* is assumed to coincide with the midship section, i.e., approximately at half the overall length. Under this assumption, the longitudinal distance between the *CG* and the location of the bow diving planes considered in the analysis is approximately 29 m. This distance is subsequently used to define the relative longitudinal position of the diving planes with respect to the global reference system of the submarine.

Since the objective of the study is to investigate the influence of the relative position of the bow diving planes on the structural behaviour of the hull–plane connection, several geometric details that do not significantly affect the local structural response are omitted. Consequently, appendages and secondary external features not directly involved in the load-transfer mechanism are excluded from the numerical representation. The external hull geometry is therefore idealised while preserving the overall dimensions, the characteristic hull curvature in the region under investigation, and the relative position of the diving planes. This simplification reduces the computational cost while retaining the geometric parameters governing the structural response of the hull–plane connection.

3.2. Bow Diving Plane Geometry and Structural Configuration

The bow diving planes considered in the present study are located on both sides of the forward region of the submarine and are arranged symmetrically with respect to the longitudinal centreline. Based on the reference system defined in the previous section, their longitudinal position is approximately 29 m from the assumed centre of gravity of the submarine. The rotation axis of each plane is oriented in the transverse direction, allowing

the hydrodynamic forces generated by the control surface to produce the pitching moment required for depth control. For the numerical analysis, the external geometry of each diving plane is idealised by means of a trapezoidal planform. The span, measured from the hull connection to the plane tip, is set to 2 m, while the root and tip chords are 1.2 m and 0.8 m, respectively. Accordingly, the reference planform area, S, is 2.0 m^2. The resulting taper ratio, defined as the ratio between the tip and root chords, is $\lambda = 0.667$, whereas the corresponding aspect ratio is $AR = 2$. The mean aerodynamic chord is approximately 1.013 m and is located at a spanwise distance of approximately 0.467 m from the root section.

The structural connection between the diving plane and the submarine hull is established through a transverse bracket located in the root region of the plane (Figure 2). This bracket constitutes the main load-transfer path between the diving plane and its supporting structure and is therefore subjected to the forces and moments resulting from the hydrodynamic loading acting on the control surface. The bracket is manufactured from steel, with the following mechanical properties: $E = 206$ GPa, $\nu = 0.3$, $\sigma_{yield} = 235$ MPa and $\rho = 7850$ kg/m^3. Its geometry is defined by height h, width m and thickness t, with two 15 mm heel dimensions, adopted to ensure sufficient clearance for the specified fillet weld throat, together with a 35 mm scallop, in accordance with Bureau Veritas design requirements [27]. The internal connection between the hull and the diving plane is represented according to the structural arrangement shown in Figure 2.

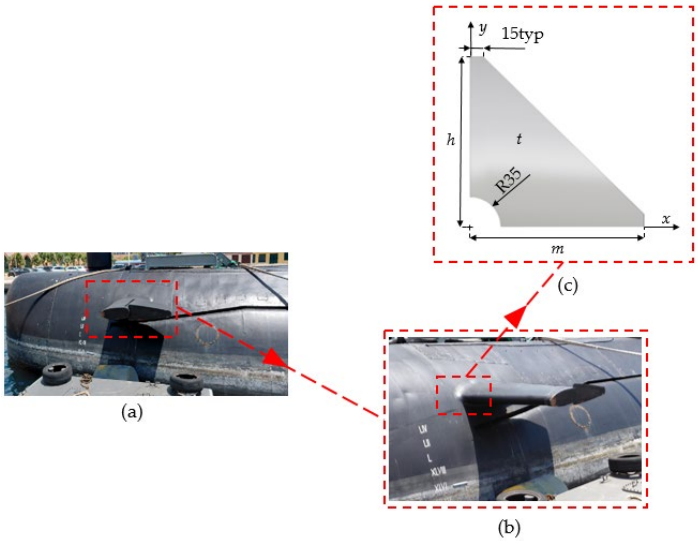


Figure 2. (**a**) Port bow diving plane, (**b**) connection between the diving plane and the submarine hull, (**c**) load-transfer bracket.

A reference velocity of 5 m/s, corresponding to approximately 9.72 knots, is considered for the definition of the hydrodynamic loading. The resulting load acting on the diving plane is subsequently transferred through the supporting structure and submarine hull (corner bracket). Table 1 summarizes the different bracket configurations considered, together with their corresponding dimensions.

Table 1. Geometric dimensions of the bracket configurations.

$h \times m$ (mm)	t (mm)	Notation
200 × 200 250 × 250 300 × 300 350 × 350 400 × 400	10, 11, 12, 13, and 14	$h \times m \times t$

The bracket is reinforced with flat-bar stiffeners positioned along its edges and plate faces, following one of the configurations illustrated in Figure 3.

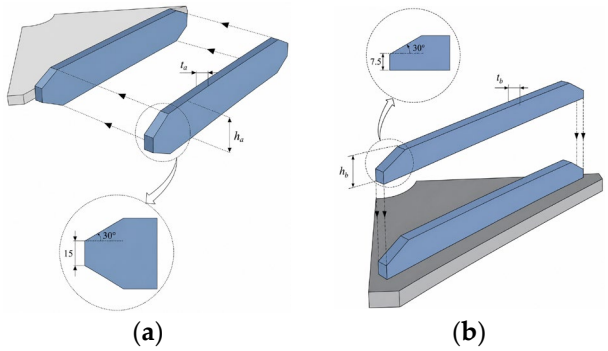


Figure 3. Stiffener configurations (all dimensions in mm): (**a**) model *a*; (**b**) model *b*.

In configuration *a*, a symmetrical face plate is welded along the free edge of the bracket. Its ends are sniped and tapered at 30°, with a 15 mm offset measured above the heels [28]. Configuration *b* employs a flat bar welded to the bracket face, positioned 15 mm from the free edge and above the heels. Its ends are likewise sniped and tapered at 30°, in accordance with DNV recommendations [29]. Both configurations are described by the stiffener height (h_a and h_b) and thickness (t_a and t_b). Table 2 summarizes the different reinforcing flat-bar configurations considered, based on the dimensions defining each stiffening method.

Table 2. Scantlings of the stiffening configurations.

Method *a*		**Method *b***		**Nomenclature**
h_a **(mm)**	t_a **(mm)**	h_b **(mm)**	t_b **(mm)**	
40	10, 11, 12, 13, 14	20	10, 11, 12, 13, 14	$\gamma h_\gamma \times t_\gamma$
45		22.5		
50		25		
55		27.5		

Where γ identifies the stiffening method considered (a or b).

4. Numerical Approach

The finite element representation illustrated in Figure 4 was developed in ANSYS® Workbench 2021 to evaluate buckling resistance. For this preliminary investigation, the constitutive response is restricted to the elastic regime, with geometric changes treated within a small-displacement framework. Through-thickness stress variations are examined using a discretisation comprising tetrahedral and three-dimensional solid elements [30]. Mesh refinement follows the methodology described by [31], while element dimensions vary progressively across adjacent regions to avoid abrupt changes in discretization density.

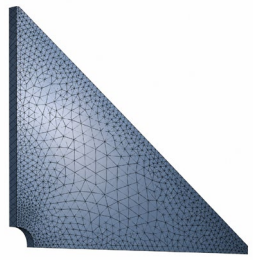


Figure 4. Mesh discretization.

The bracket is modelled with simply supported boundary conditions along its supported edges, while the compressive loading is applied along the bracket edges in the plane of the plate to investigate its elastic buckling response. At this stage of the investigation, welds are not explicitly modelled; their restraining effect is idealised through the adopted simply supported boundary conditions, a conventional simplification in preliminary plate-buckling analyses. The numerical investigation is restricted to linear-elastic buckling under the prescribed loading conditions. Initial geometric imperfections, material plasticity, welding-induced residual stresses and fatigue effects are not considered. Consequently, the results are intended to compare the relative elastic buckling resistance of the investigated bracket geometries and stiffening arrangements, rather than to establish the ultimate strength or operational safety of the complete hull–plane connection.

The convergence of the unstiffened bracket solution with respect to the finite element discretisation was examined by progressively refining the mesh. For each mesh configuration, the change in von Mises stress relative to the previous discretisation was calculated and compared with the accuracy requirements reported by Patil and Jeyakarthikeyan [32]. The refinement process was terminated once the stress variation satisfied the most stringent criterion considered. Table 3 presents the results obtained for the different mesh densities. Based on this assessment, the mesh was progressively refined up to 2180 elements and 4765 nodes, for which the variation in von Mises stress with respect to the preceding discretisation was reduced to 0.75%. This refined discretisation was therefore adopted for the numerical assessment.

Table 3. Mesh sensitivity analysis.

	σ_{VM} (MPa)	Variation (%)	Nodes	Elements
1	46.7	-	383	167
2	63.27	26.18	1261	561
3	74.94	15.57	3294	1497
4	75.5	0.75	4765	2180

The mesh-refinement assessment presented in this study is based on the von Mises stress response of the unstiffened reference bracket and does not constitute a convergence verification of the elastic buckling load multiplier, MA. Although a consistent finite-element modelling approach is adopted for the investigated configurations, this consistency alone does not establish the mesh independence of their respective buckling load multipliers. Consequently, the numerical values of MA and the percentage differences reported between configurations should be interpreted as results obtained at the adopted discretisation level, rather than as mesh-converged estimates of critical buckling resistance. The comparisons are therefore intended to identify preliminary trends associated with changes in bracket geometry and stiffening arrangement. A dedicated mesh-refinement assessment based on MA, performed for the reference and stiffened configurations, would be necessary to establish the numerical convergence and robustness of the reported buckling improvements.

The hydrodynamic and finite-element analyses address complementary aspects of the hull–diving-plane load path, but they are not connected through an explicit quantitative load-transfer procedure in the present model. The analytical formulation provides the resultant hydrodynamic loading and the corresponding bending moment at the diving-plane root, whereas the finite-element assessment examines the elastic buckling response of the hull-side bracket under prescribed in-plane compressive loading. The root bending moment is not directly converted into an equivalent compressive load or spatial load distribution applied to the bracket. Such a conversion would require a detailed representation of the intervening structural load path, including the connection geometry, load-bearing mem-

bers and associated force and moment equilibrium. Accordingly, the finite-element results should be interpreted as a comparative assessment of bracket geometries and stiffening arrangements under a common idealised structural loading condition, rather than as a direct prediction of the bracket response to the calculated hydrodynamic root bending moment. Establishing this quantitative correspondence would require an extended structural model and a specifically defined load-transfer procedure.

5. Results and Discussion

5.1. Effects of Bow-Plane Position and Angle of Attack on the Pitching Moment

The reference longitudinal distance between the bow diving planes and the fixed, mid-length centre of gravity is estimated as $d = 29$ m from the general arrangement of the submarine, assuming that the centre of pressure coincides longitudinally with the identified plane position. The hydrodynamic force acting on each plane is evaluated assuming a seawater density of $\rho = 1025$ kg/m^3, an operating speed of $U = 5$ m/s, a plane area of $S = 2$ m^2 and the linear lift relation $C_L = 4.19\alpha$, with α expressed in radians. To directly compare the relative influence of longitudinal position and angle of attack on pitching-moment generation, both parameters are varied by ±10% about the reference condition $d_0 = 29$ m and $\alpha_{ref} = 4°$, using intermediate 5% increments (Figure 5).

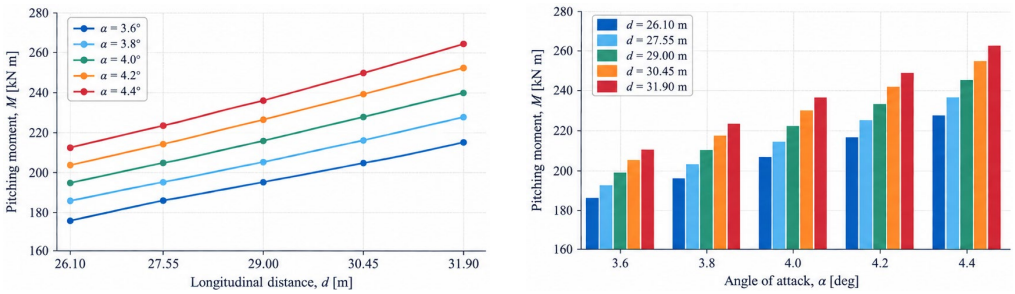


Figure 5. Influence of bow-plane position and angle of attack on the pitching moment. (**a**) Effect of longitudinal position (varying d at fixed α), (**b**) effect of angle of attack (varying α at fixed d).

The results show that longitudinal plane position and angle of attack exhibit the same relative sensitivity in terms of pitching-moment generation within the investigated range. Under the adopted linear model, a 10% increase in either d or α, with all other variables held constant, produces a corresponding 10% increase in pitching moment. Their simultaneous increase by 10% leads to a 21% moment gain, from 217.38 to 263.03 kN·m per plane, as a consequence of the multiplicative dependence of M on d and α.

Although equivalent in terms of pitching-moment sensitivity, the two parameters are not equivalent from a structural-load perspective. Starting from the reference condition ($d_0 = 29$ m and $\alpha_{ref} = 4°$), increasing the longitudinal distance by 10% to 31.9 m raises the pitching moment from 217.38 to 239.11 kN·m while the hydrodynamic force transmitted through the plane–hull connection remains unchanged at 7.50 kN. The same pitching moment can be obtained without modifying the plane position by increasing the angle of attack by 10%, from 4.0° to 4.4°; however, this alternative increases the transmitted force to 8.25 kN. Consequently, for the same pitching moment of 239.11 kN·m, the forward-positioned plane requires approximately 9.1% less transmitted force than the increased-incidence configuration.

This result reveals an important distinction between pitching-moment authority and structural loading. Increasing the moment arm enhances pitching-moment generation without increasing the hydrodynamic force that must be transferred through the plane–hull

connection, whereas increasing incidence achieves the same moment gain through a proportional increase in hydrodynamic loading. Longitudinal position therefore determines the inherent moment-generation efficiency of the configuration, while angle of attack provides the operational control required to modulate the resulting pitching moment. From a design perspective, this distinction suggests that, where geometric and integration constraints allow, increasing the longitudinal moment arm can reduce the connection load required to achieve a prescribed pitching moment. Position and incidence should therefore not be regarded as interchangeable design variables, despite their equivalent relative sensitivity in terms of pitching moment, but rather as complementary geometric and operational mechanisms.

It should be emphasised that the longitudinal-position sensitivity investigated in this section isolates the geometric effect of the moment arm under unchanged local hydrodynamic conditions. The finite-element assessment is performed for the reference configuration at d = 29 m and examines the influence of connection geometry and stiffening under the prescribed reference loading. Consequently, the present results do not represent a fully resolved structural comparison of diving planes installed at different longitudinal positions. Such an extension would require position-dependent local inflow conditions and load distributions to be determined and subsequently transferred to the corresponding structural models.

From a practical design perspective, the longitudinal distance d should not be regarded as a fixed property of the diving-plane location alone, since the submarine centre of gravity varies with the loading and trim condition. For a candidate bow-plane position, the corresponding moment arm should therefore be evaluated over the expected CG operating envelope associated with variations in fuel and consumables, weapon or payload state, and trim-tank management. The present framework can then be applied to representative loading conditions to determine the corresponding control-force requirement and transmitted structural demand. Selection of the longitudinal position would consequently be based on its performance over the relevant operating envelope rather than on a single nominal CG location, while also accounting for arrangement and hydrodynamic constraints beyond the scope of the present model.

5.2. Effects of Operating Depth and Speed on Local Incidence Speed

The coupled influence of operating depth and local incident speed is investigated through the angle of attack required to preserve a prescribed pitching moment. This formulation provides a direct measure of how changes in the surrounding hydrostatic and hydrodynamic conditions translate into control-surface incidence requirements. The longitudinal distance between the diving-plane centre of pressure and the fixed submarine centre of gravity is maintained at $d = 29$ m, with an exposed planform area of $S = 2$ m^2 per plane. A reference operating condition is defined at a depth of 50 m, a local incident speed of 5 m/s and an angle of attack of $\alpha_{ref} = 4°$. All forces and moments are reported for a single plane; for a symmetric pair subjected to identical loading, the resulting contribution is twice the reported value.

To isolate the effect of pressure-induced density variation from changes in seawater composition and temperature, an idealised water column is considered with constant absolute salinity of 35 g/kg and conservative temperature of 10 °C. Sea pressure is obtained from depth at a reference latitude of 45° using the standard GSW conversion, and the corresponding in-situ density is evaluated according to TEOS-10 [33]. The resulting thermodynamic profile is deliberately idealised and is therefore intended to isolate the physical contribution of pressure-dependent density rather than reproduce the hydrographic conditions of a particular operating area [34]. Within these assumptions, the analysis enables the individual

and combined effects of operating depth and incident speed on the incidence required to preserve a constant pitching moment to be quantified.

A systematic 6 × 5 parametric matrix is therefore constructed by combining six operating depths, from 50 to 300 m in 50 m increments, with five local incident speeds of 4.5, 4.75, 5, 5.25 and 5.5 m/s. The resulting 30 operating conditions are used to determine the angle of attack required to preserve the reference pitching moment (217.38 kN·m), thereby enabling the individual and combined influence of depth and incident speed to be quantified. The complete parametric matrix, including the pressure-dependent seawater density calculated at each depth, is reported in Table 4 and Figure 6.

Table 4. Parametric matrix of the angle of attack required to preserve the reference pitching moment of 217.38 kN·m per plane as a function of operating depth and local incident speed.

Depth (m)	Density (kg/m^3)	4.5 m/s	4.75 m/s	5 m/s	5.25 m/s	5.5 m/s
50	1027.052	4.9383	4.4321	4	3.6281	3.3058
100	1027.279	4.9372	4.4312	3.9991	3.6273	3.3051
150	1027.505	4.9361	4.4302	3.9982	3.6265	3.3043
200	1027.732	4.9350	4.4292	3.9974	3.6257	3.3036
250	1027.958	4.9339	4.4282	3.9965	3.6249	3.3029
300	1028.184	4.9328	4.4273	3.9956	3.6241	3.3021

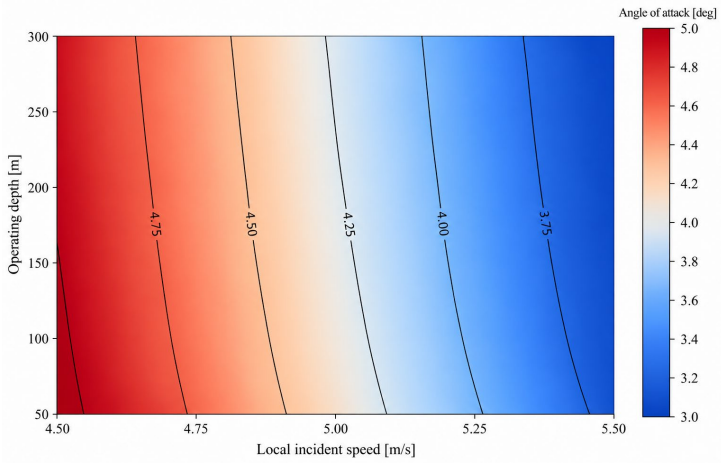


Figure 6. Contour map of the angle of attack required to preserve the reference pitching moment of 217.38 kN·m per plane as a function of operating depth and local incident speed.

The parametric analysis reveals a pronounced separation between the effects of operating depth and local incident speed on the incidence required to preserve the reference pitching moment. As shown by the near-vertical iso-incidence contours, the response is governed predominantly by incident speed, whereas pressure-induced density variations with depth introduce only a comparatively weak correction within the investigated operating envelope. At the reference speed of 5 m/s, increasing the operating depth from 50 to 300 m reduces the required angle of attack only from 4° to 3.9956°. In contrast, at 50 m depth, decreasing the local incident speed from 5 to 4.5 m/s increases the required incidence to 4.9383°, while increasing it to 5.5 m/s reduces the required incidence to 3.3058°. The markedly different responses demonstrate that, under the present assumptions, variations in local incident speed dominate the control-incidence requirement, while the effect associated with pressure-induced density variation remains secondary. This behaviour follows directly from the governing hydrodynamic relationship rather than representing

an empirical coincidence of the selected cases. For fixed pitching moment, plane area, longitudinal moment arm and lift-curve slope, the required incidence scales as

$$\alpha_{req} \propto \frac{1}{\rho U_e^2} \tag{13}$$

Consequently, the logarithmic sensitivities of the required incidence to density and incident speed are $\partial \ln \alpha_{req} / \partial \ln \rho = -1$ and $\partial \ln \alpha_{req} / \partial \ln U_e = -2$, respectively. A given relative perturbation in incident speed therefore produces, locally, twice the relative response associated with an equivalent perturbation in density. The contrast becomes substantially greater over the present operating envelope because the two variables do not undergo comparable relative changes: between 50 and 300 m, the calculated in-situ density increases by only approximately 0.1103%, resulting in a 0.1101% reduction in required incidence at fixed speed, whereas the investigated speed range extends ±10% about the reference condition. The nonlinear character of the speed dependence is also evident from the asymmetric incidence response to symmetric speed perturbations. A 10% reduction in incident speed, from 5 to 4.5 m/s, requires an incidence increase of 23.46%, whereas a 10% increase to 5.5 m/s permits a 17.36% reduction. This asymmetry is the direct consequence of the inverse-square dependence $\alpha_{req} \propto U_e^{-2}$: equal positive and negative percentage changes in speed cannot produce equal and opposite incidence corrections. This result is particularly relevant from an operational perspective, since loss of local incident speed imposes a disproportionately larger incidence demand than the reduction obtained from an equivalent relative speed increase.

The pressure-induced increase in seawater density provides only a limited compensating effect when incident speed decreases. At 4.50 m/s, increasing depth from 50 to 300 m reduces the required incidence from 4.9383° to 4.9328°. The additional density associated with depth therefore recovers only a small fraction of the incidence demand generated by the reduction in dynamic pressure. Within the idealised water column considered here, neglecting pressure-induced density variation would introduce an incidence difference of approximately 0.11% between the shallowest and deepest conditions. This establishes density variation with depth as a second-order correction for the present sensitivity analysis, rather than a controlling parameter of the required incidence.

An additional consequence emerges when these results are interpreted from a structural perspective. Because both the prescribed pitching moment and the longitudinal moment arm are fixed, the resultant hydrodynamic force required from each plane also remains fixed at approximately 7.5 kN throughout the parametric matrix. Changes in speed and density are therefore accommodated, within the adopted model, by changes in incidence rather than by changes in the resultant force required to generate the prescribed moment. This produces a clear distinction between control demand and resultant structural load: substantially different operating conditions may require markedly different plane incidences while preserving the same resultant force transmitted through the plane–hull connection. This invariance applies only to the resultant lift represented by the present formulation and should not be extrapolated to invariance of the local structural response. Changes in pressure distribution, drag, torsional loading, viscous effects and detailed hull–plane interaction are not resolved and may modify the local stress state even when the resultant pitching moment is unchanged.

The present results should therefore be interpreted as a quantified sensitivity assessment within the defined operating envelope rather than as a universal hierarchy between depth and speed effects. The predominance of incident speed arises from both its quadratic role in the hydrodynamic loading and the comparatively small pressure-induced density variation generated by the idealised 50–300 m water column. Nevertheless, within these explicitly defined assumptions, the analysis establishes a robust result: maintaining

pitching-moment authority across changes in operating condition is primarily an incidence-management problem driven by local incident speed, with pressure-induced density variation acting only as a minor correction. Extension of the analysis to measured temperature–salinity profiles, validated installed-plane lift characteristics and resolved hull–plane interaction would enable this sensitivity framework to be translated to submarine-specific operating conditions.

5.3. Effects of Diving-Plane Aspect Ratio

The influence of diving-plane aspect ratio is investigated through a controlled geometric comparison in which the exposed planform area and prescribed pitching moment are maintained constant. Three trapezoidal planforms are considered, with exposed spans of 1.6, 2 and 2.5 m. For each configuration, the root and tip chords are adjusted while preserving an exposed area of $S = 2$ m^2 per plane and a constant taper ratio of two-thirds. This formulation redistributes an identical lifting area between span and chord, thereby isolating the hydrodynamic effect associated with planform slenderness from changes attributable simply to lifting-surface area. The resulting geometries are summarised in Table 5.

Table 5. Geometric definition of the diving-plane configurations used to isolate the effect of aspect ratio (span denotes the exposed distance from the hull-side root to the plane tip).

Nomenclature	Span, b (m)	Root Chord, cr (m)	Tip Chord, ct (m)	Area, S (m^2)
Short-span	1.6	1.5	1	2
Reference	2	1.2	0.8	2
Long-span	2.5	0.96	0.64	2

The hydrodynamic operating condition is held fixed throughout the comparison. The local incident speed is 5 m/s, the longitudinal distance between the plane centre of pressure and the fixed submarine centre of gravity is 29 m, and the in-situ seawater density is 1027.052 kg/m^3, corresponding to the previously defined idealised water column at 50 m depth. A prescribed pitching moment of 217.38 kN·m per plane is imposed, which, for the fixed moment arm, defines a common resultant lift requirement of approximately 7.5 kN. The longitudinal centre-of-pressure location is deliberately retained across all geometries so that differences in hydrodynamic response arise from the redistribution of planform geometry rather than from changes in moment arm. A symmetric section, small incidence, and attached flow are assumed. Consistent with the preliminary planar-symmetry representation of the hull adopted in the present model, each exposed diving plane is reflected about its root. The resulting equivalent lifting surface therefore has twice the exposed span and twice the exposed area. Aspect ratio and the corresponding finite-span lift-curve slope are subsequently evaluated for each configuration using this equivalent lifting-surface representation [35].

The hydrodynamic effect of the geometric redistribution is introduced through the equivalent aspect ratio of the lifting surface. Under the adopted planar-symmetry representation, reflection of each exposed plane about the hull-side root gives an equivalent span $2b$ and an equivalent area $2S$. The corresponding aspect ratio is therefore

$$AR_{eq} = \frac{2b^2}{S} \tag{14}$$

This equivalent reflected-surface representation is an idealisation and should not be interpreted as an exact hydrodynamic representation of a diving plane installed on a real submarine hull. In particular, it does not resolve the hull boundary layer, wake-induced non-uniformity or finite hull–appendage interaction, all of which may modify the effective aspect ratio and local loading of the installed plane.

The finite-span lift-curve slope is then estimated from

$$a = \frac{2\pi}{1 + 2/AR_{eq}}, \; C_L = a{\cdot}\alpha \tag{15}$$

where b denotes the exposed span, S is the exposed area of one plane and α is expressed in radians. An idealised span-efficiency factor of unity is adopted in this preliminary formulation. Because S is identical for all three configurations, increasing b increases AR without introducing an accompanying change in lifting area. The resulting variation in a can therefore be attributed directly to the finite-span effect associated with planform slenderness. For the prescribed pitching moment and fixed longitudinal moment arm, the required resultant lift F is common to all configurations. Combining the linear lift relation with the dynamic-pressure formulation gives the incidence required to generate this force:

$$\alpha_{req} = \frac{2F}{\rho {U_e}^2 Sa} \tag{16}$$

This expression establishes the first consequence of increasing aspect ratio. At fixed F, ρ, U_e and S, the required incidence varies inversely with the finite-span lift-curve slope. Increasing span at constant area therefore increases the lifting effectiveness of the plane and reduces the incidence required to generate the prescribed pitching moment. Importantly, this comparison isolates a geometric efficiency effect: neither additional lifting area nor an increased longitudinal moment arm contributes to the predicted reduction in incidence. The same geometric modification, however, also alters the structural leverage of the hydrodynamic load about the hull-side connection. To quantify this competing effect within a common analytical framework, an elliptical spanwise lift distribution is prescribed (Figure 7):

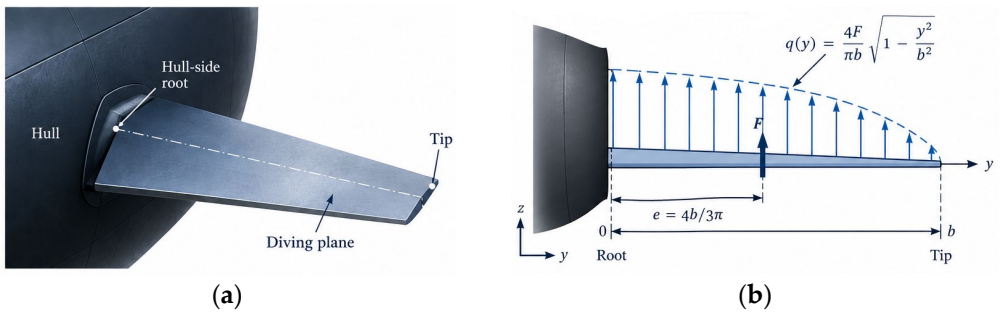


Figure 7. Spanwise lift distribution: (**a**) isometric view, (**b**) side view.

And hence the corresponding root bending moment is $M_r = Fe = \frac{4Fb}{3\pi}$.

These relationships expose the central geometric trade-off examined in this section. Increasing span at constant planform area increases the equivalent aspect ratio and finite-span lift-curve slope, thereby reducing the incidence required to generate a prescribed pitching moment. At the same time, the resultant hydrodynamic force acts through a larger effective spanwise lever arm, causing the bending moment transmitted at the hull-side root to increase linearly with exposed span. Aspect ratio therefore cannot be interpreted solely as a measure of hydrodynamic effectiveness: under a fixed-area constraint, the same geometric modification that improves incidence efficiency simultaneously increases the structural leverage imposed on the plane–hull connection.

The combined hydrodynamic and structural consequences of the geometric variation are summarised in Table 6. The comparison is performed under identical planform area, prescribed pitching moment, and resultant lift force, thereby isolating the influence of diving-plane geometry on the required incidence and root bending moment (M_r).

Table 6. Hydrodynamic and structural response of the diving-plane configurations at constant planform area and prescribed pitching moment, showing the influence of equivalent aspect ratio on required incidence and root bending moment.

Configuration	Equivalent Aspect Ratio	Required Angle (Deg)	Lift Force (kN)	Root Bending Moment (kN·m)
Short-span	2.56	4.75	7.511	5.1
Reference	4	4	7.511	6.38
Long-span	6.25	3.52	7.511	7.97

The root bending moments reported in Table 6 are conditional on the assumed elliptical spanwise lift distribution. No sensitivity analysis with alternative load distributions is performed in the present study. A different spanwise distribution would modify the location of the resultant lift and therefore the absolute root bending moment. Consequently, the reported values and percentage variations should be interpreted within this common loading assumption rather than as universal predictions for an installed diving plane. Determination of the actual spanwise loading would require higher-fidelity hydrodynamic analysis including hull–appendage interaction.

The results reveal a clear hydrodynamic–structural trade-off associated with increasing diving-plane aspect ratio under a fixed-area constraint. Relative to the reference configuration ($b = 2$ m, $AR_{eq} = 4$), increasing the exposed span to 2.5 m raises the equivalent aspect ratio to 6.25 and reduces the incidence required to generate the prescribed pitching moment from 4.00° to 3.52°, corresponding to a reduction of approximately 12%. However, this hydrodynamic benefit is accompanied by a 25% increase in root bending moment, from 6.38 to 7.97 kN·m. The opposite response is obtained for the short-span configuration: reducing the exposed span to 1.60 m decreases AR_{eq} to 2.56 and the root bending moment to 5.10 kN·m (−20%), but increases the required incidence to 4.75° (+18.75%). Percentage variations are evaluated from the unrounded values; the tabulated reference incidence is reported as 4°. The opposing trends originate from two distinct consequences of the same geometric modification. Hydrodynamically, increasing span at constant planform area raises the equivalent aspect ratio and, within the adopted finite-span formulation, increases the lift-curve slope by reducing the finite-span incidence penalty. The prescribed lift can therefore be generated at a lower angle of attack. Structurally, however, the same increase in span shifts the resultant hydrodynamic load farther from the hull-side root. Because the assumed elliptical distribution places the resultant at $e = 4b/(3\pi)$, the effective load arm scales directly with exposed span and, for the common resultant force, the root bending moment consequently satisfies $M_r \propto b$. The reduction in required incidence and the increase in root bending moment are therefore not contradictory responses, but simultaneous manifestations of the same change in planform geometry.

A particularly significant result emerges from the fact that the resultant lift remains essentially unchanged at 7.511 kN for all three configurations. If hydrodynamic force alone were used as a proxy for structural demand, the configurations would appear equivalent. The root-moment assessment demonstrates that they are not: the long-span plane transmits the same resultant lift while producing a 25% larger bending moment at the hull-side connection than the reference configuration. Conversely, the short-span plane reduces this bending moment by 20% despite requiring substantially greater incidence. Constant resultant force therefore does not imply constant structural demand when the spatial distribution and lever arm of that force are altered.

This distinction has direct implications for diving-plane design. Increasing aspect ratio improves the incidence efficiency with which a prescribed pitching moment is generated, but this improvement is not structurally neutral: under the present fixed-area formulation,

it is obtained at the cost of increased bending leverage at the plane–hull connection. Conversely, reducing span alleviates root bending demand while requiring greater incidence to recover the same control authority. Aspect ratio therefore acts as a coupling parameter between hydrodynamic effectiveness and structural load transmission rather than as an exclusively hydrodynamic design variable. The results consequently preclude identifying either extreme configuration as intrinsically superior: selection of span must balance the incidence required to achieve the prescribed control moment against the associated root bending demand. More broadly, the comparison demonstrates why the structural consequences of diving-plane geometry cannot be inferred from resultant hydrodynamic force alone. Two configurations delivering identical pitching authority and transmitting the same resultant lift may impose substantially different demands on the hull–plane connection solely because of how that load is distributed in space. Within the assumptions of the present model, the hydrodynamic gain associated with increasing aspect ratio is therefore accompanied by an inherent structural leverage penalty, establishing the need to consider hydrodynamic effectiveness and local load transmission concurrently when assessing diving-plane geometry.

5.4. Structural Response of the Hull–Diving Plane Connection

The preceding sections establish the hydrodynamic load path from diving-plane operation to the bending demand developed at the hull-side root. The final stage of the analysis addresses the receiving structure itself. The plane–hull connection is represented by an internal bracket located immediately inboard of the diving-plane root, through which the root bending moment M_r is transferred into the surrounding hull structure. This final assessment therefore closes the load path considered in the present work: hydrodynamic force generation, pitching-moment authority, root bending moment and, finally, local structural response of the bracket connection. The buckling resistance of the internal bracket at the hull-side root is investigated through controlled variations in its principal geometric parameters, namely the arm length, height, and plate thickness. The elastic buckling response is evaluated using the load multiplier factor provided by ANSYS Workbench, denoted here as MA. This dimensionless parameter represents the factor by which the prescribed reference load must be multiplied to obtain the predicted critical elastic buckling load. Higher MA values therefore indicate greater predicted elastic buckling resistance under the same reference loading and boundary conditions. MA should not be interpreted as the displacement amplitude of the buckling mode or as a measure of ultimate structural strength. Consequently, larger *MA* values indicate a greater margin against elastic instability, whereas lower values denote an earlier onset of buckling under an equivalent reference load (Figure 8).

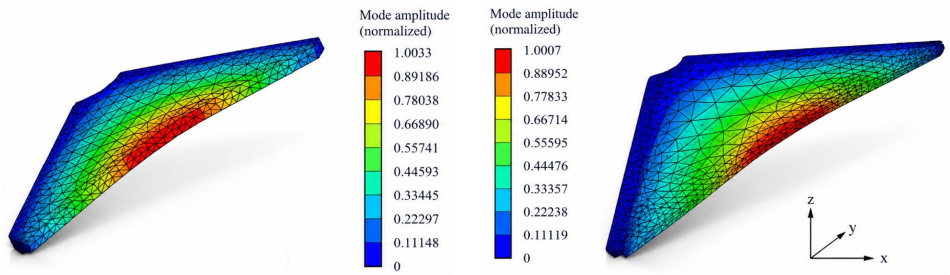


Figure 8. Influence of bracket geometry on the predicted elastic buckling mode for different combinations of arm length, height and thickness. (**a**) 250 × 250 × 13, (**b**) 400 × 400 × 10.

A remarkably consistent buckling pattern is observed throughout the investigated geometric domain. Variations in bracket arm, height, and thickness primarily modify the critical buckling moment, *MA*, without fundamentally altering the governing instability mode. For most unstiffened configurations, the maximum stress remains concentrated at the scallop–deck-beam intersection, shifting towards the scallop–web-frame intersection only for the largest 400 × 400 mm brackets with thicknesses of 12–14 mm. In contrast, the maximum displacement consistently occurs at the mid-length of the free edge. Thus, bracket geometry predominantly governs the resistance to instability rather than the nature of the buckling mechanism itself, with only the stiffest configurations exhibiting a local redistribution of the critical stress region. Figure 9 shows the evolution of *MA* and bracket weight for a fixed arm length and height of 200 mm, considering different plate thicknesses.

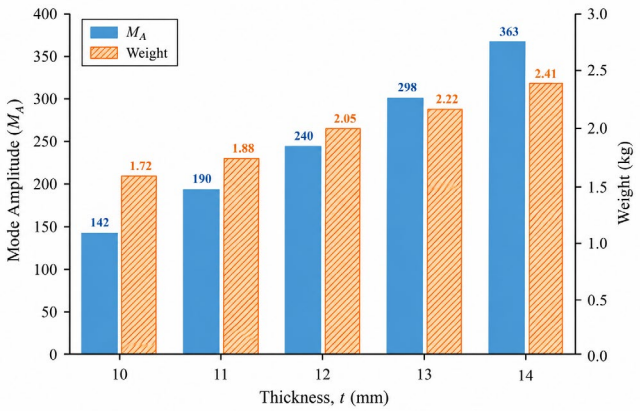
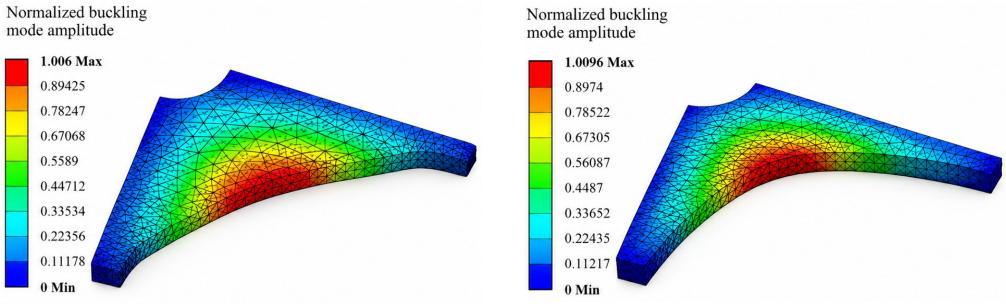


Figure 9. Influence of bracket plate thickness on *MA* and structural weight for the 200 × 200 mm unstiffened configuration, highlighting the progressive enhancement in elastic buckling resistance and the associated weight penalty.

Increasing the bracket thickness provides the most direct means of enhancing its elastic buckling resistance, as reflected by the corresponding increase in *MA*. This improvement, however, is necessarily accompanied by additional structural weight. Although the relative increase in mass remains smaller than the associated gain in buckling resistance within the investigated range, thickness enlargement represents an essentially material-driven solution. Consequently, two alternative geometric strategies are investigated to determine whether the stability response can be improved more efficiently through a redistribution of the bracket geometry. The first strategy replaces the original straight free edge with a continuously curved profile, thereby modifying the stiffness distribution without altering the fundamental bracket topology. Curvature radii of 200, 300 and 400 mm are evaluated for each baseline bracket geometry. The second strategy retains a predominantly straight free edge but introduces soft toes at the intersections with the web frame and deck beam, each extending 12.5% of the corresponding bracket arm and height. The two transitions are connected to the straight free edge through curvature radii of 40, 50, and 60 mm. These configurations provide a controlled basis for assessing whether local reshaping of the free-edge region can delay the onset of elastic instability more effectively than a uniform increase in plate thickness. Figure 10 illustrates representative buckling modes obtained for the two geometric modifications.

A systematic evaluation of all geometric combinations confirms the superior performance of the soft-toe configuration. Compared with the continuously curved free-edge alternative, the soft-toe solution achieves a 38.1% greater improvement in buckling resistance while simultaneously reducing structural weight by 2.9%. This combined response is particularly significant, as the enhanced stability is obtained through a more effective redistribution

of the bracket geometry rather than through additional material, identifying the soft-toe transition as the more structurally efficient of the two geometric strategies investigated.



(**a**) (**b**)

Figure 10. Representative elastic buckling mode shapes for the proposed free-edge geometries: (**a**) 300 × 300 × 12 mm bracket with soft-toe transitions and a 40 mm curvature radius; (**b**) 200 × 200 × 12 mm bracket incorporating a continuously curved free edge with a 200 mm radius.

A complementary strategy for enhancing the elastic buckling resistance is the introduction of dedicated stiffening elements, which modify the load-transfer mechanism without requiring a uniform increase in bracket thickness. Figure 11 compares the resulting buckling modes for the investigated stiffening concepts at their minimum scantlings with that of the unstiffened bracket at the maximum thickness considered. This deliberately demanding comparison provides a direct assessment of whether targeted reinforcement can outperform a material-intensive increase in plate thickness.

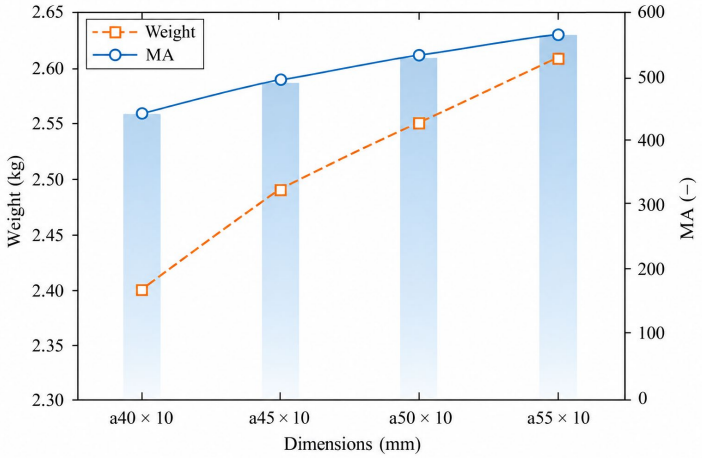


Figure 11. Influence of reinforcing flat-bar dimensions on MA and structural weight, illustrating the coupled evolution of buckling response and weight penalty with increasing stiffener size.

Table 7 provides a direct quantitative comparison between the method *a* (200 × 200 × 10.a40 × 10) and method *b* (200 × 200 × 10.b20 × 10) stiffened configurations at their minimum scantlings and the unstiffened bracket at the maximum thickness considered (14 mm), using *MA* and structural weight as the principal performance metrics.

Table 7. Structural performance comparison of the investigated stiffening strategies and the unstiffened reference configuration.

	Non-Stiffened	**Method *a***	**Method *b***
Weight (kg)	2.41	2.40	2.06
MA	363.84	437.75	668.58

It should be noted that the comparison is intentionally performed between different material-distribution strategies rather than between brackets of identical plate thickness. The unstiffened reference configuration has dimensions of 200 × 200 × 14 mm, whereas the stiffened configurations use a thinner 200 × 200 × 10 mm baseline bracket supplemented by the corresponding reinforcing flat bar. Method *b* (200 × 200 × 10.b20 × 10) therefore achieves a lower total weight (2.06 kg versus 2.41 kg) while increasing *MA* from 363.84 to 668.58, corresponding to an 83.8% increase. This comparison illustrates the greater efficiency of targeted material placement relative to a uniform increase in bracket thickness under the modelling assumptions adopted.

Irrespective of the stiffening strategy, targeted reinforcement provides a more structurally efficient solution than increasing the thickness of the unstiffened bracket, achieving greater buckling resistance at a lower structural weight. Relative to the 14 mm unstiffened configuration, the method *a* and method *b* stiffening strategies increase *MA* by 20.3% and 83.8%, respectively. This confirms that the stability response is governed not only by the amount of material employed, but also by its effective distribution within the bracket. Figure 11 further illustrates the dimensional sensitivity of the stiffening concept by showing the influence of increasing reinforcing flat-bar dimensions on *MA* and structural weight. The corresponding comparison between the two stiffening strategies is provided quantitatively in Table 7.

Increasing either the height or thickness of the reinforcing flat bar produces a systematic increase in *MA*, confirming the direct contribution of stiffener dimensions to the buckling response. The parametric assessment indicates an approximately linear evolution of MA and structural weight over the investigated dimensional range, illustrating the predictable trade-off between enhanced buckling resistance and the associated material penalty.

6. Conclusions

This study has established a sequential hydrodynamic–structural framework for assessing bow diving planes in which control effectiveness is traced through the complete load path, from hydrodynamic force generation and pitching-moment authority to root bending and, ultimately, the elastic stability of the hull–plane connection. The results demonstrate that quantities that appear equivalent from a global hydrodynamic perspective may lead to markedly different structural consequences at the attachment. This distinction constitutes the central outcome of the investigation and highlights the need to treat diving-plane position, geometry, operating condition, and structural integration as interconnected design variables rather than as independent considerations.

Under the adopted linear formulation, longitudinal position and angle of attack exhibit identical relative sensitivities with respect to pitching-moment generation. However, their structural implications are fundamentally different. A 10% increase in longitudinal moment arm increases the pitching moment by 10% without modifying the transmitted hydrodynamic force, whereas obtaining the same moment increase through incidence requires a proportional increase in force. For the investigated reference configuration, the forward-positioned plane therefore generates the same 239.11 kN·m pitching moment with approximately 9.1% less transmitted force than the increased-incidence alternative. This establishes longitudinal positioning as a geometric mechanism for increasing moment authority per unit transmitted force, while incidence remains the operational mechanism through which that authority is modulated.

Operating conditions introduce a second, clearly differentiated sensitivity. Within the idealised 50–300 m water column, pressure-induced density variation has only a minor influence on the incidence required to preserve pitching authority, whereas local incident speed is dominant. At 5 m/s, increasing depth from 50 to 300 m changes the required inci-

dence only from 4° to 3.9956°. Conversely, at 50 m depth, a 10% reduction in speed increases the required incidence by 23.46%, while a 10% speed increase reduces it by 17.36%. Thus, within the investigated operating envelope, preservation of pitching-moment authority is primarily an incidence-management problem governed by local dynamic pressure rather than by pressure-induced changes in seawater density.

The geometric study further shows that hydrodynamic efficiency cannot be used as a surrogate for structural efficiency. Increasing the equivalent aspect ratio from 4.00 to 6.25 reduces the incidence required for the prescribed pitching moment by approximately 12%, but simultaneously increases the root bending moment by 25%. Conversely, the short-span configuration reduces root bending by 20% at the expense of an 18.75% increase in required incidence. Most significantly, all three configurations transmit essentially the same resultant lift of 7.511 kN, yet develop substantially different root bending moments. Consequently, constant resultant force does not imply constant structural demand: the spatial distribution of that force and its effective lever arm are equally decisive. Aspect ratio therefore emerges as a genuine hydrodynamic–structural coupling parameter rather than an exclusively hydrodynamic descriptor.

At the connection level, the parametric finite-element assessment demonstrates that structural performance is governed not only by the amount of material employed but, critically, by where that material and stiffness are introduced. Increasing bracket thickness improves elastic buckling resistance but does so through a direct weight penalty. Geometric redistribution provides a more efficient alternative: across the complete set of investigated combinations, the soft-toe configuration achieves a 38.1% greater improvement in buckling resistance than the continuously curved free-edge solution while reducing structural weight by 2.9%. Targeted stiffening strengthens this conclusion. Even at their minimum scantlings, both investigated stiffening strategies outperform the 14 mm unstiffened bracket while reducing weight; the corresponding increases in MA reach 20.3% and 83.8% for methods a and b, respectively. Increasing flat-bar dimensions subsequently produces an approximately linear increase in both MA and structural weight, providing a predictable means of tuning the stability margin against material penalty.

Taken together, these findings reveal a consistent design principle: the effectiveness of a bow diving plane cannot be established from pitching authority, hydrodynamic force, or structural strength in isolation. Increasing the longitudinal lever arm can improve moment generation without increasing transmitted force; increasing aspect ratio can reduce incidence while simultaneously amplifying root bending; and increasing structural mass is not necessarily the most effective route to improving connection stability. The governing design problem is therefore one of load-path management, in which hydrodynamic authority must be generated and transmitted through the diving plane while controlling the mechanical demand ultimately received by the hull-side connection.

The present results are intentionally derived within a controlled numerical framework designed to isolate the investigated mechanisms and should therefore be interpreted within the assumptions adopted in this study. In particular, the conclusions regarding operating depth and speed are restricted to the idealised water column, environmental conditions and analytical hydrodynamic formulation considered, while the observed effects of aspect ratio are dependent on the adopted fixed-area planform, finite-span correction and idealised spanwise load distribution. Similarly, the conclusions concerning bracket geometry and stiffening are restricted to the linear-elastic structural model, prescribed boundary and loading conditions, and investigated geometric configurations. Accordingly, the quantitative results should not be extrapolated directly to arbitrary submarine configurations or operating conditions. Future work should extend the analysis towards resolved hull–plane hydrodynamic interaction, experimentally or CFD-validated installed-plane characteristics, realistic

temperature–salinity profiles, nonlinear structural behaviour and hydroelastic coupling. Nevertheless, within these assumptions, the relationships identified provide a consistent basis for examining the interaction between bow-plane location, planform geometry and connection architecture.

Author Contributions: Conceptualization, A.S.-C. and F.P.-A.; methodology, A.S.-C. and F.P.-A.; software, A.S.-C. and M.A.H.-S.; validation, F.P.-A. and M.A.H.-S.; formal analysis, A.S.-C. and F.P.-A.; investigation, A.S.-C. and F.P.-A.; resources, A.S.-C.; data curation, F.P.-A.; writing—original draft preparation, A.S.-C. and M.A.H.-S.; writing—review and editing, F.P.-A. and M.A.H.-S.; visualization, A.S.-C. and F.P.-A.; supervision, F.P.-A. and M.A.H.-S.; project administration, A.S.-C. and F.P.-A. All authors have read and agreed to the published version of the manuscript.

Funding: This research received no external funding.

Institutional Review Board Statement: Not applicable.

Informed Consent Statement: Not applicable.

Data Availability Statement: All data are presented in the paper.

Acknowledgments: The authors would like to acknowledge the support received from the Universidad Politécnica de Madrid.

Conflicts of Interest: The authors declare no conflicts of interest.

References

1. Berté, L.; Piaggio, B.; Scotto, L.; Becchetti, S.; Viviani, M.; Villa, D. Development of a CFD-Based Submarine Manoeuvrability Prediction Code. In *Technology and Science for the Ships of the Future, Proceedings of the 21st International Conference on Ships and Maritime Research (NAV 2025), Messina, Italy, 18–20 June 2025*; SAGE Publications: Thousand Oaks, CA, USA, 2025; pp. 262–272.
2. Renilson, M. *Submarine Hydrodynamics*, 2nd ed.; Springer: Cham, Switzerland, 2018.
3. Renilson, M. Influence of the L/D ratio on the rotary coefficients of a submarine. *J. Mar. Sci. Technol.* **2023**, *28*, 615–623. [CrossRef]
4. Andrews, D. Submarine Design. In *Encyclopedia of Maritime and Offshore Engineering*; Wiley: Hoboken, NJ, USA, 2017. [CrossRef]
5. Eyiler, B.; Bayraktarkatal, E. Investigation of Optimum Structures at Submarine Pressure Hulls under Hydrostatic Pressure with Finite Element Method. *J. Nav. Archit. Mar. Technol.* **2024**, *226*, 25–35. [CrossRef]
6. Dubbioso, G.; Broglia, R.; Zaghi, S. Submarine Manoeuvrability Design: Traditional Cross-Plane vs. X-Plane Configurations in Intact and Degraded Conditions. *J. Mar. Sci. Eng.* **2022**, *10*, 2014. [CrossRef]
7. Ward, J.C.; Harwood, C.M.; Young, Y.L. Inverse method for hydrodynamic load reconstruction on a flexible surface-piercing hydrofoil in multi-phase flow. *J. Fluids Struct.* **2018**, *77*, 58–79. [CrossRef]
8. Young, Y.L.; Garg, N.; Brandner, P.A.; Pearce, B.W.; Butler, D.; Clarke, D.; Phillips, A.W. Load-dependent bend-twist coupling effects on the steady-state hydroelastic response of composite hydrofoils. *Compos. Struct.* **2018**, *189*, 398–418. [CrossRef]
9. Kim, D.-H.; Kim, J.; Baek, H.-M.; Choi, Y.-M.; Shin, J.-H.; Lee, J.; Shin, S.-C.; Shin, Y.-H.; Chae, E.J.; Kim, E.S.; et al. Experimental investigation on a generic submarine hydrodynamic model considering the interaction effects of hull motion states and control planes. *Ocean Eng.* **2024**, *298*, 116878. [CrossRef]
10. Lee, S.-K.; Jones, M.B.; Quick, H. Loads and hull-pressure measurements on a generic submarine in different stages of model build-up. *Ocean Eng.* **2023**, *271*, 113677. [CrossRef]
11. Zaghi, S.; Di Mascio, A.; Broglia, R.; Muscari, R. Application of dynamic overlapping grids to the simulation of the flow around a fully-appended submarine. *Math. Comput. Simul.* **2015**, *116*, 75–88. [CrossRef]
12. Phillips, A.B.; Furlong, M.; Turnock, S.R. The use of computational fluid dynamics to aid cost-effective hydrodynamic design of autonomous underwater vehicles. *Proc. Inst. Mech. Eng. Part M J. Eng. Marit. Environ.* **2010**, *224*, 239–254. [CrossRef]
13. Jagadeesh, P.; Murali, K.; Idichandy, V.G. Experimental investigation of hydrodynamic force coefficients over AUV hull form. *Ocean Eng.* **2009**, *36*, 113–118. [CrossRef]
14. Khan, K.; Korulla, M.; Nagarajan, V.; Sha, O.P. Measurements of steady manoeuvring forces and moments over an axisymmetric body with appendages in a wind tunnel. *Ship Technol. Res.* **2024**, *72*, 23–34. [CrossRef]
15. Phan, T.L.; Mai, T.L.; Nguyen, T.T. Computational Fluid Dynamics Investigation of Hydrodynamic Forces and Moments Acting on Stern Rudder Plane Configurations of a Submarine. *Appl. Sci.* **2024**, *14*, 4292. [CrossRef]
16. Han, J.; Jung, J.; Lee, S.; Jang, G.; Lee, S. Dynamic Stability Analysis of a Submarine by Changing Conning Tower Position and Control Planes. *J. Navig. Port Res.* **2017**, *41*, 389–394. [CrossRef]

17. Shariati, S.K.; Mousavizadegan, S.H. The effect of appendages on the hydrodynamic characteristics of an underwater vehicle near the free surface. *Appl. Ocean Res.* **2017**, *67*, 31–43. [CrossRef]
18. Cheng, Y.; Liu, T.; Liu, J. Topology optimization of ship bracket structures. *Chin. J. Ship Res.* **2015**, *10*, 53–58+70. [CrossRef]
19. Smith, M.J.; Macadam, T.; MacKay, J.R. Integrated modelling, design and analysis of submarine structures. *Ships Offshore Struct.* **2015**, *10*, 349–366. [CrossRef]
20. MacKay, J.R.; van Keulen, F. Partial safety factor approach to the design of submarine pressure hulls using nonlinear finite element analysis. *Finite Elem. Anal. Des.* **2013**, *65*, 1–16. [CrossRef]
21. Paik, J.K.; Thayamballi, A.K.; Kim, B.J. Finite element modelling and strength analysis of hold No. 1 of bulk carriers. *Ocean Eng.* **2004**, *31*, 2129–2152.
22. Xu, M.C.; Yanagihara, D.; Fujikubo, M.; Soares, C.G. Influence of boundary conditions on the collapse behaviour of stiffened panels under combined loads. *Mar. Struct.* **2013**, *34*, 205–225. [CrossRef]
23. Kim, K.-S.; Roh, M.-I.; Ha, S. Expert system based on the arrangement evaluation model for the arrangement design of a submarine. *Expert Syst. Appl.* **2015**, *42*, 8731–8744. [CrossRef]
24. Kim, K.-S.; Roh, M.-I. A submarine arrangement design program based on the expert system and the multistage optimization. *Adv. Eng. Softw.* **2016**, *98*, 97–111. [CrossRef]
25. Kim, S.; You, Y.; Lee, S. Optimization of volumes and longitudinal locations of trim and compensation tanks for underwater vehicles using non-dominated sorting genetic algorithm II. *Int. J. Nav. Archit. Ocean Eng.* **2026**, *18*, 100740. [CrossRef]
26. Li, J.; Rao, Z.; Su, J.; Qu, Y.; Hua, H. A numerical method for predicting the hydroelastic response of marine propellers. *Appl. Ocean Res.* **2018**, *74*, 188–204. [CrossRef]
27. Massachusetts Institute of Technology. Unified Engineering, F9 Lecture Notes: "Lift Slope Reduction"; *MIT OpenCourseWare*, 2005–2006. p. 4. Available online: https://ocw.mit.edu/courses/16-01-unified-engineering-i-ii-iii-iv-fall-2005-spring-2006/345c18f1f9b58b42301e8b1731abe3c8_f09_0304.pdf (accessed on 1 September 2026).
28. Bureau Veritas. Pt B, Chapter 11, Appendix 2. Sheets for Special Structural Details. 2022. Available online: https://rulesexplorer.bureauveritas.com/publication (accessed on 1 September 2026).
29. Bureau Veritas. Pt B, Chapter 4, Section 3. Strength Principles; Section 4. Bottom Structure; Section 5. Side Structure. 2022. Available online: https://rulesexplorer-docs.bureauveritas.com/documents/nr467/jul2026/467-NR_PartB_2026-07.pdf#page (accessed on 1 September 2026).
30. DNVGL. Rules for Classification, Part 3 Hull, Chapter 3 Structural Design Principles, Section 6. 2017. Available online: https://rulesexplorer.bureauveritas.com/publication (accessed on 1 September 2026).
31. Tveiten, B.W.; Moan, T. Determination of structural stress for fatigue assessment of welded aluminum ship details. *Mar. Struct.* **2000**, *13*, 189–212. [CrossRef]
32. Kim, J.; Jeom, J.; Park, J.; Seo, H.; Ahn, H.; Lee, J. Effect of reinforcement on buckling and ultimate strength of perforated plates. *Int. J. Mech. Sci.* **2015**, *92*, 194–205. [CrossRef]
33. Patil, H.; Jeyakarthikeyan, P.V. Mesh convergence study and estimation of discretization error of hub in clutch disc with integration of ANSYS. *IOP Conf. Ser. Mater. Sci. Eng.* **2018**, *402*, 012065. [CrossRef]
34. TEOS-10. gsw_rho: In-Situ Density (75-Term Equation). Available online: https://www.teos-10.org/pubs/gsw/html/gsw_rho.html (accessed on 1 September 2026).
35. TEOS-10. gsw_p_from_z: Pressure from Height. Available online: https://www.teos-10.org/pubs/gsw/pdf/p_from_z.pdf (accessed on 7 September 2026).

Disclaimer/Publisher's Note: The statements, opinions and data contained in all publications are solely those of the individual author(s) and contributor(s) and not of MDPI and/or the editor(s). MDPI and/or the editor(s) disclaim responsibility for any injury to people or property resulting from any ideas, methods, instructions or products referred to in the content.